



Article

Regional Characteristics of Cloud Properties over the Loess Plateau

Shuhua Zhang ^{1,*}, Cunyin Jin ¹, Qianqian Tian ¹, Xueqian Ding ¹ and Guanghui Ming ²¹ College of Geomatics, Xi'an University of Science and Technology, Xi'an 710054, China² Key Laboratory of Water Management and Water Security for Yellow River Basin, Ministry of Water Resources, Yellow River Engineering Consulting Co., Ltd., Zhengzhou 450003, China

* Correspondence: shuhuazhang@xust.edu.cn

Abstract: As an important meteorological element, clouds play an important role in the radiative transfer process and atmospheric and water circulation. The Loess Plateau is the largest arid and semi-arid area in China, with a fragile ecological environment. However, few scholars have studied the spatial and temporal variations in cloud properties in the Loess Plateau. Therefore, in this study, cloud properties in the Loess Plateau were analyzed at the annual, seasonal, and diurnal scales based on Himawari-8 cloud products. The results show that cloud frequency (CF), cloud optical thickness (COT) and cloud effective radius (CER) show obvious spatial discrepancies in the Loess Plateau. Regions with high CF and COT values are mainly concentrated in the southern part of the Loess Plateau. In general, areas with high CER values also have low COT values. The highest CF values are observed in summer, and the highest COT values mainly appear in autumn. However, the highest CER values mainly appear in spring and winter. In terms of the diurnal variation, the CF is high at midday and low in the morning and afternoon, while the diurnal variation in COT values is the opposite: there are high COT values in the morning and afternoon and low values at midday. The CER values show an increasing trend from morning to afternoon and reach a maximum at 17:00 BJT. High CF values in the southern Loess Plateau and in summer relate to surface water and heat conditions; the vegetation cover, total column water vapor and temperature values are relatively high in this area. High COT values in the southern Loess Plateau are associated with sufficient water vapor levels and high levels of aerosol optical thickness. However, high CER levels in the northern Loess Plateau and in spring and winter may be caused by a higher nucleation rate related to the colder temperature. Moreover, more factors could influence CER, i.e., water vapor and aerosols, but they show complex relationships with the CER which need further explored.

Keywords: cloud frequency; cloud optical thickness; cloud effective radius; Himawari-8

Citation: Zhang, S.; Jin, C.; Tian, Q.; Ding, X.; Ming, G. Regional Characteristics of Cloud Properties over the Loess Plateau. *Remote Sens.* **2023**, *15*, 2603. <https://doi.org/10.3390/rs15102603>

Academic Editors: Bao-Jie He, Linchuan Yang and Junqing Tang

Received: 26 April 2023

Accepted: 15 May 2023

Published: 17 May 2023



Copyright: © 2023 by the authors. Licensee MDPI, Basel, Switzerland. This article is an open access article distributed under the terms and conditions of the Creative Commons Attribution (CC BY) license (<https://creativecommons.org/licenses/by/4.0/>).

1. Introduction

Clouds usually appear with high frequency, and they cover about 60% of the Earth [1]. They influence the Earth's energy balance by absorbing or emitting longwave radiation and reflecting or scattering shortwave radiation [2,3]. Slight changes in the macro- or micro-properties of clouds have significant effects on radiation balance, energy balance, interactions between the atmosphere and the surface, and even climate change [4–6]. Therefore, spatio-temporal variations in cloud properties are fundamental to our understanding of the mechanisms of cloud radiative forcing effects, so as to more effectively evaluate the role of clouds in radiation balance and climate change [7].

To capture the temporal and spatial variations in cloud properties, different detection methods and datasets have been used. The most straightforward way to observe cloud changes is manually from the ground, which was the only way to measure cloud cover in the past. Today, cloud properties and cloud fractions can be determined automatically from the ground, e.g., with a total sky imager (TSI) covering the entire hemispherical sky [8].

However, ground stations are sparsely and unevenly distributed, and the representation of ground stations is weak in regional studies [9]. With the development of remote sensing, an effective method of cloud detection has emerged. The macro- and micro-properties of clouds can be inverted based on different sensors. Clouds and the Earth's Radiant Energy System (CERES) and International Satellite Cloud Climatology Project (ISCCP) both produce cloud datasets based on remote sensing data; they focus on cloud and radiation parameters, and the projects began in the early stages, i.e., in 1982 for ISCCP and in 1998 for CERES. Although updated versions of CERES (Edition 4) and ISCCP-FH have been released in recent years, they still have coarse resolutions of about 110 km, and they are not suitable for use in regional studies [10–12]. With the development of sensors and with an increasing number of satellites being launched, cloud datasets based on individual satellites or combinations of different satellites have been released, and their spatial resolutions have been improved. Examples include products of MO(Y)D06 from the polar-orbiting satellite based on sensor of Moderate Resolution Imaging Spectroradiometer (MODIS), and Patmos-X (Pathfinder Atmospheres–Extended) which was produced by integrating more observations from an Advanced Very High-Resolution Radiometer (AVHRR) flown on different satellites. Geostationary satellites such as Himawari-8, Geostationary Operational Environmental Satellite (GOES) and Meteosat Second Generation (MSG) also provide cloud products [13–15]. Cloud datasets based on polar-orbiting satellites or geostationary satellites have relatively high spatial resolutions, i.e., the spatial resolutions of MOD06 and Himawari-8 are 1 km and 5 km, respectively. The Cloud Aerosol Lidar and Infrared Satellite Observation (CloudSat) satellite with an active cloud profile radar (CPR) and the Cloud-Aerosol Lidar with Orthogonal Polarization (CALIOP) on board the Cloud Aerosol Lidar Infrared Pathfinder Observation (CALIPSO) satellite can provide vertical cloud structures, meaning that CloudSat and CALIPSO are better methods of capturing the 3D structures of clouds, such as cloud top height, cloud base height and the number of cloud layers, but the temporal resolutions of CloudSat and CALIPSO are too low to capture temporal variations in clouds [16–18]. By comparing different cloud products from different satellites, we can conclude that clouds inverted by sensors on polar-orbiting satellites and geostationary satellites are both suitable for regional cloud characteristic analysis because they both represent clouds with relatively high spatial and temporal resolutions. In addition, cloud datasets from geostationary satellites have higher temporal resolutions than those from polar-orbiting satellites, making them suitable for diurnal variation analysis.

Cloud cover and cloud microphysical properties have regional characteristics which influence the regional radiative balance and local climate, which also involve cloud formation [19,20]. For example, Liu [21] and Wang et al. [18] found that the distribution of cloud properties has significant regional characteristics over the Tibetan Plateau: the cloud optical thickness and cloud water paths decrease from the southeast to the northwest. Zhou et al. [22] also found that the cloud occurrence frequency over the Tibetan Plateau is higher from evening to midnight and reaches the minimum value in the morning. In the Loess Plateau (LP), unique land-surface processes and land–atmosphere interactions take place, because it is the transition zone from plain to plateau, crossing arid, semi-arid and semi-humid zones, and climate change has been significant in recent years [23]. In addition, in the Loess Plateau, land cover has also changed significantly due to the implementation of ecological restoration projects that altered land–atmosphere processes in this area [24–26]. Therefore, to enhance our comprehension of local atmospheric circulation, land–atmosphere interactions and local climate change, we investigated the temporal and spatial characteristics of clouds over the Loess Plateau. Diurnal variation in clouds regulates the diurnal changes in longwave and shortwave radiation flux and precipitation, which helps us to better understand the regional characteristics of radiation budget, climate and even local meteorology. We analyzed the annual, seasonal and diurnal features of clouds, and Himawari-8 cloud products were used because of their higher temporal resolutions with 10 min. The potential factors that affect the spatial and temporal characteristics of clouds were also discussed. These findings can help us to understand changes in the

local cloud–radiation–climate system and the process of local atmospheric circulation and regional climate change over the Loess Plateau.

2. Materials and Methods

2.1. Research Area

The Loess Plateau is located in the north–central part of China ($100^{\circ}52'E$ – $114^{\circ}31'E$, $33^{\circ}41'N$ – $41^{\circ}16'N$), with an altitude of 84 m to 5206 m above sea level (Figure 1) [27]. It is the largest area of loess accumulation in the world. There are thousands of ravines in this area, which are fragmented and form typical landforms such as the Yuan, Liang and Mao loess [28]. In terms of climate type, it has a semi-humid and semi-arid climate, with most of the precipitation concentrated in the summer [29]. In most areas of the Loess Plateau, the aerosol optical thickness has obvious inter-annual variation, and the largest dust aerosol load occurs in spring. The annual average temperature and precipitation values in the whole region also have obvious spatial discrepancies: they are higher in the southern part than in the northern part of the Loess Plateau [30,31].

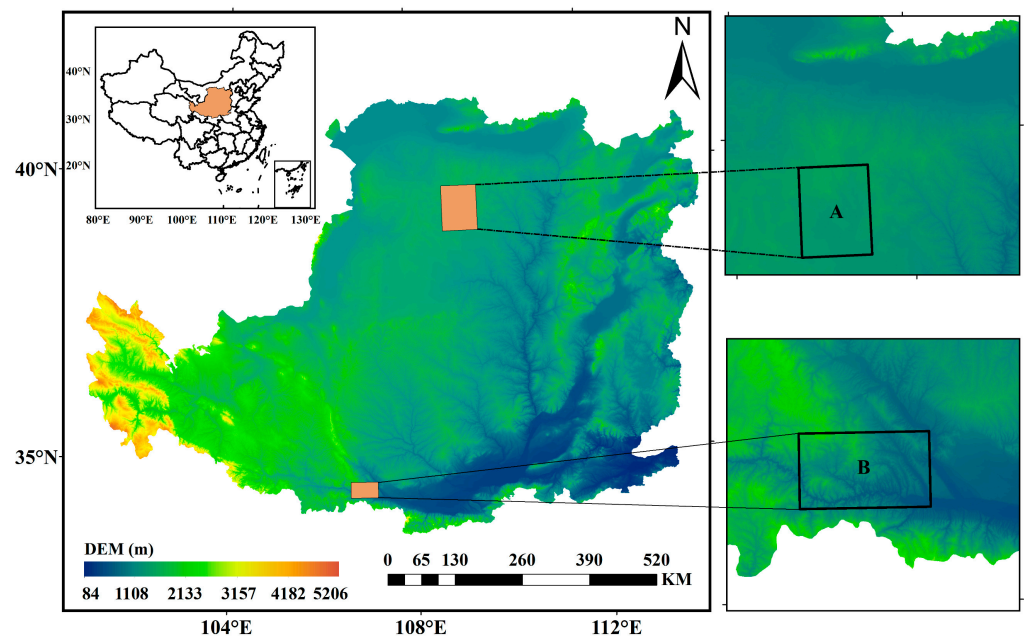


Figure 1. Location and digital elevation model (DEM) of the Loess Plateau and two sub-regions (A,B).

2.2. Himawari-8 Satellite Cloud Products

Himawari-8 (H-8) is a new-generation geostationary satellite operated by the Japan Meteorological Agency, equipped with the Advanced Himawari Imager (AHI) sensor. It was launched around $140^{\circ}E$ above the equator on 17 October 2014, but it started running in 2015 [32]. The spatial coverage of H-8 is $60^{\circ}N$ – $60^{\circ}S$, $80^{\circ}E$ – $160^{\circ}W$, and it acquires data every 10 min for the full disk [33]. Compared with sensors on polar-orbiting satellites, such as MODIS and AVHRR, observations from H-8 have higher temporal and spatial resolutions [34]. Products based on the H-8 satellite can be downloaded for free from <http://www.eorc.jaxa.jp/ptree/>, accessed on 19 June 2022. In this study, we used the H-8 cloud products of cloud optical thickness and cloud effective radius. They both have a temporal resolution of 10 min and a spatial resolution of 5 km. We selected data from July 2015 to February 2022 for our analysis. Details of the dataset are shown in Table 1.

Table 1. List of data used in this study and relevant details.

Data Source	Datasets/Parameters	Temporal Resolution	Spatial Resolution	Download
Himawari-8	Cloud optical thickness (COT); cloud effective radius (CER)	10 min	5 km	https://www.eorc.jaxa.jp/ptree/ , accessed on 19 June 2022
CloudSat (2B-CLDCLASS-LIDAR)	Cloud phase	16 d	2.5 km (along-track) × 1.4 km (cross-track)	http://www.cloudsat.cira.colostate.edu/ , accessed on 16 November 2022
ECMWF(ERA5)	Total column water vapor (TCWV)	Hourly	0.25° × 0.25°	https://cds.climate.copernicus.eu/ , accessed on 9 January 2023
NASA(MERRA2)	Aerosol optical thickness (AOT)	Hourly	0.5° × 0.625°	https://disc.gsfc.nasa.gov/ , accessed on 6 January 2023
MODIS (MOD13A3)	Normalized difference vegetation index (NDVI)	Monthly	1 km	https://ladsweb.modaps.eosdis.nasa.gov/ , accessed on 27 December 2022
National Tibetan Plateau Data Center	Temperature (TMP)	Monthly	1 km	http://data.tpdc.ac.cn/ , accessed on 26 December 2022
National Tibetan Plateau Data Center	Potential evapotranspiration (PET)	Monthly	1 km	http://data.tpdc.ac.cn/ , accessed on 26 December 2022

2.3. Ancillary Datasets

To better explain the temporal and spatial distribution characteristics of clouds, we selected the total column water vapor, representing the water content condition in the atmosphere; the normalized difference vegetation index; temperature; potential evapotranspiration; and the aerosol optical thickness, representing the conditions of surface water, heat and aerosols to determine the possible reasons for regional cloud characteristics over the Loess Plateau. Details of the auxiliary dataset are also shown in Table 1.

2.4. Methods

In this study, we used the H-8 cloud dataset from July 2015 to February 2022. Annual, seasonal and diurnal variations in cloud optical thickness, cloud effective radius and cloud frequency were analyzed. Seasons were separated based on spring (March–May), summer (June–August), autumn (September–November) and winter (December–February). To clearly show the diurnal variation, the time we used was Beijing Standard Time (BJT) (UTC + 8). Due to the limitations in Advanced Himawari Imager (AHI) observations, H-8 only provides daytime cloud products [7]. According to the sunrise and sunset times in the four seasons, we selected 7:00–18:00 BJT in spring and summer, 7:00–17:00 BJT in autumn and 8:00–17:00 BJT in winter as the daytime.

Although there is no cloud frequency dataset in H-8, we calculated the cloud frequency (CF) on the space and time scales. To capture the distribution of CF, we calculated CF in the specific time period for every pixel (see Equation (1)). For example, an annual CF map was created by dividing the number of cloud occurrence times by the total number of observation times in a year for every pixel. However, to determine the CF at the temporal scale, firstly, we calculated the spatial CF by dividing the number of cloud pixels by the total number of pixels in the region, and the average spatial CF was used as the mean CF in the corresponding time period (see Equation (2)). To determine the cloud optical thickness (COT) and cloud effective radius (CER), they were averaged in space or time to present the temporal changes and spatial distribution, respectively.

The cloud frequency in time and space can be calculated as follows:

$$CF_{i,j} = \frac{N_{cloud-tp,i,j}}{N_{T,i,j}} \quad (1)$$

$$CF_T = \frac{\sum_{t=1}^{N_T} (N_{cloud,t} / N_{total,t})}{N_T} \quad (2)$$

where $CF_{i,j}$ is the cloud frequency for a pixel with the position of (i, j) . $N_{cloud-tp,i,j}$ is the number of cloud occurrences for the calculated time period at the pixel and $N_{T,i,j}$ is the number of observed instances during the calculated time period at the same pixel. CF_T is the mean CF in a specific time period. $N_{cloud,t}$ is the number of cloud pixels at time t , $N_{total,t}$ is the number of pixels for the whole region at time t and N_T is the total number of observed instances for the calculated time period.

To explore the relationship between potential influence factors and cloud properties, in this paper, Geodetector was used. Geodetector is a statistical tool used to measure spatial stratified heterogeneity (SSH), which refers to phenomena within the strata that are more similar than those between the strata. The Geodetector method can quantify to what extent a certain variable X can explain the spatial heterogeneity of response variable Y , and it can be used to investigate the interaction between two explanatory variables X_1 and X_2 to a response variable Y . The SSH of Y and to what extent the explanatory variable X explains the SSH of Y can be measured using the Geodetector q -statistic [35,36]:

$$q = 1 - \frac{\sum_{h=1}^L N_h \sigma_h^2}{N \sigma^2} \quad (3)$$

where q is the explanatory power of variable X on Y . The value range is $[0, 1]$, and the larger the value, the stronger the explanatory power of X on Y . $h = 1, \dots, L$ represents the strata of explanatory variable X . N_h and N are the number of units in strata h and the whole region. σ_h^2 and σ^2 are the variances in strata h and the whole region, respectively.

3. Results

3.1. Annual and Seasonal Cloud Properties over Loess Plateau

We calculated the annual and seasonal means of CF, COT and CER in space, and the results are shown in Figure 2. The spatial mean of the annual CF was 46.59%. Based on Figure 2a–e, we could see that the CF shows a similar spatial pattern: there were higher CF values in the southern Loess Plateau, and there were comparatively lower CF values in the northern Loess Plateau for all time scales. Moreover, different patterns could also be observed between the four seasons. The highest spatial mean CF value was observed in summer (63.47%), and the lowest value was observed in winter (28.00%). The spatial distribution of CF in summer showed that areas with high values were mountain ranges: Lvliang mountain and Taihang mountain over the eastern Loess Plateau and Qilian mountain over the western Loess Plateau, which indicates that topographic relief contributes to cloud generation over the Loess Plateau.

The annual and seasonal mean COT values in space are shown in Figure 2f–j. The spatial mean of the annual COT value was 18.07, and the COT values were 14.66, 18.83, 22.23 and 11.49 in spring, summer, autumn and winter, respectively. Based on Figure 2f–j, the annual and seasonal COT values showed similar patterns to CF: high COT values were observed in the southern Loess Plateau, and low COT values were observed in the northern Loess Plateau. Moreover, higher COT values were observed in autumn, and lower COT values were observed in winter. The CER spatial distribution is shown in Figure 2k–o; it can be seen that the CER values in space showed an opposite pattern to the COT values. The annual average CER was larger in the northern Loess Plateau (30.07 μm) and smaller in the southern Loess Plateau (17.70 μm). Among the four seasons, the largest spatial mean CER value was observed in winter: 27.83 μm .

3.2. Diurnal Variation in Cloud Properties over Loess Plateau

The diurnal variations in CF, COT and CER were calculated by averaging all 10 min data between 2015 and 2021 for each hour. We also calculated the yearly and seasonal diurnal variations. The yearly diurnal variation is displayed in Figure 3a. It can be seen that the CF value in the Loess Plateau was low in the morning at around 7:00–11:00 BJT and in the afternoon at around 17:00–18:00 BJT, and it was comparatively higher between 12:00 and 15:00 BJT. The maximum value of CF was observed at 15:00 BJT. However, the diurnal variation in COT was opposite to the variation in CF; higher COT values were observed in the morning and afternoon, and they were lower at midday. The CER value increased from 7:00 to 17:00 BJT, reaching a maximum value at 17:00 BJT.

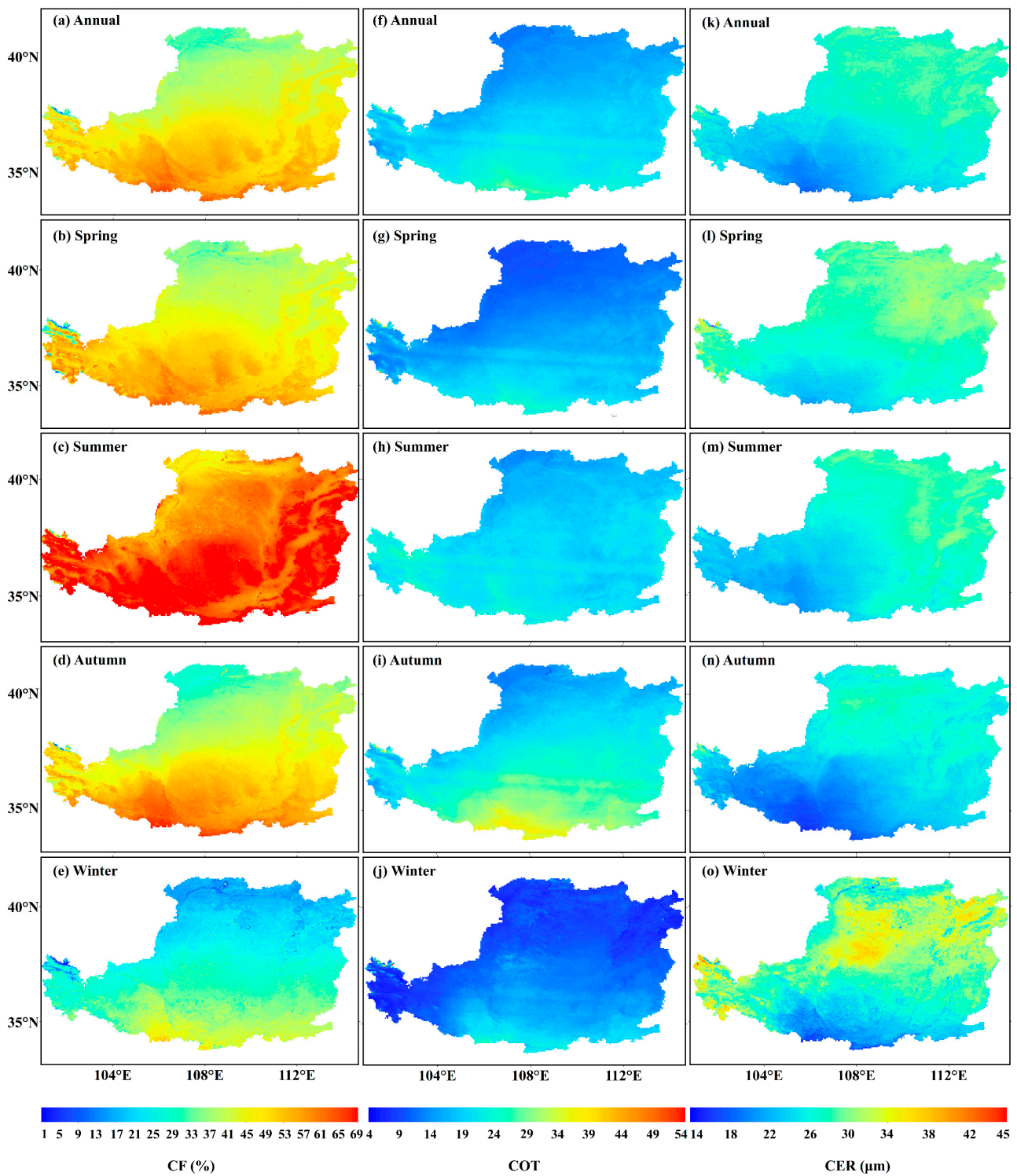


Figure 2. Spatial distribution of annual and seasonal CF, COT and CER in the Loess Plateau. CF (a–e). COT (f–j). CER (k–o).

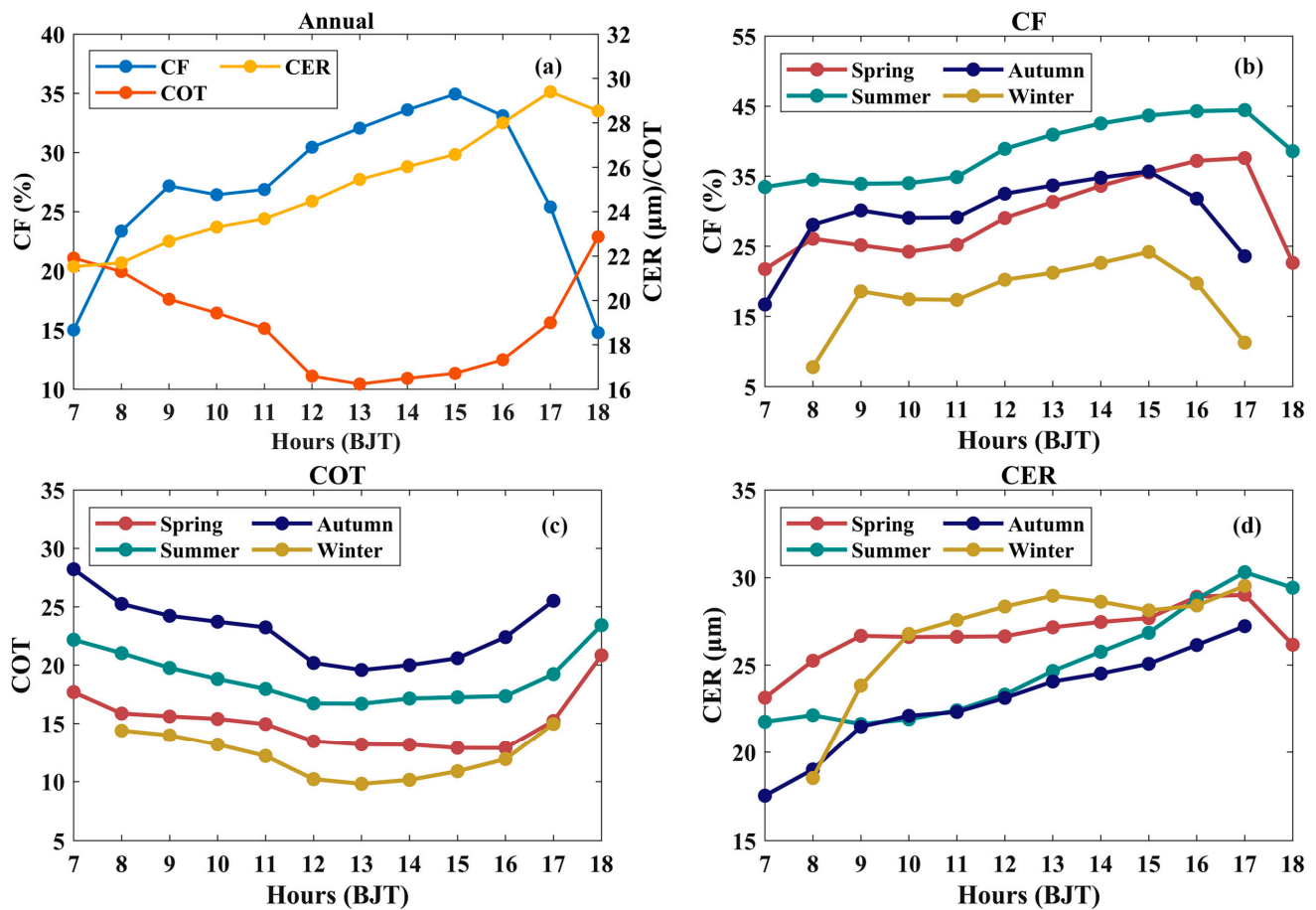


Figure 3. The diurnal variations in CF, COT and CER in the Loess Plateau. (a) Annual mean CF, COT and CER. (b) Seasonal mean CF. (c) Seasonal mean COT. (d) Seasonal mean CER.

Figure 3b–d present the diurnal variations in three cloud parameters on the Loess Plateau in four seasons. The diurnal variations in each parameter in four seasons were similar to the variation on the annual scale. However, the variation differed between the four seasons. The highest CF value was observed in summer, and the lowest was observed in winter. The CF values in autumn and spring were similar, especially at midday, around 12:00–15:00 BJT. In the comparison of the diurnal CF values in summer and winter, the largest differences between the two seasons were mainly in the morning or afternoon hours, i.e., 8:00 BJT and 17:00 BJT. From 8:00 BJT to 15:00 BJT, the CF was relatively stable, and the difference between spring and autumn was relatively small. The highest COT value was observed in autumn, and the lowest was observed in winter for all hours. Between 8:00 and 16:00 BJT, the ranking of COT values in the four seasons showed consistency with autumn > summer > spring > winter. However, the difference in COT values between the four seasons was high around midday between 12:00 and 15:00 BJT and relatively low around 8:00–10:00 BJT and 16:00–17:00 BJT, especially in spring and winter. Although the CER values in the four seasons showed an increasing trend from morning to afternoon, which is similar to the annual mean for CER, the differences between seasons were also significant in the morning, at midday and in the afternoon. In the morning, at 7:00 BJT, the CER values were similar in spring and summer, and they were similar in autumn and winter at 8:00 BJT. However, in summer and autumn, there were similar CER values between 9:00 BJT and 14:00 BJT; the same went for the CER in spring and winter between the same times. After 14:00 BJT, the CER values in the four seasons were similar.

3.3. Spatial Characteristics of Diurnal Cloud over Loess Plateau

To further explore the spatial distribution of diurnal cloud properties, we separated daytime into three periods. From 7:00 to 11:00 BJT was classed as morning time, 12:00 BJT to 15:00 BJT was classed as midday, and 16:00 BJT to 18:00 BJT was classed as afternoon. Based on all of the overpass times, we calculated the average values of cloud properties using all observations for the period between 2015 and 2021, and the results are shown in Figure 4. As can be seen from Figure 4a–c, there were lower CF values in the morning (38.94%) and afternoon (40.02%) and higher values at midday (53.68%). There was a north–south contrast in CF in the three time periods, and an obvious spatial trend was observed at midday. The CF values over the entire Loess Plateau were greater than 5.37%, and the maximum value reached 75.53% at midday. High CF values were mainly concentrated over mountain ranges: Taihang mountain and Lvliang mountain. The COT value (Figure 4d–f) showed a similar spatial trend to CF, but it was not as obvious as that of CF. COT showed higher values in the morning (20.29) and afternoon (19.73) and lower values at midday (16.51). Moreover, the maximum COT values mainly appeared in the morning in the southern part of the Loess Plateau, while the COT value of the whole area at noon was less than 28. In contrast to the COT value, the diurnal variation in CER showed a different pattern (Figure 4g–i). In the afternoon, most of the Loess Plateau showed a relatively large CER value, with a maximum CER value of 33.38 μm . Comparing the three periods, we could see that the higher CER value in the afternoon (28.65 μm) was mainly distributed in the eastern part of the Loess Plateau. Meanwhile, we could conclude that the areas with low values of CER were generally consistent with the areas with high values of COT by comparing the distribution of the COT and CER values.

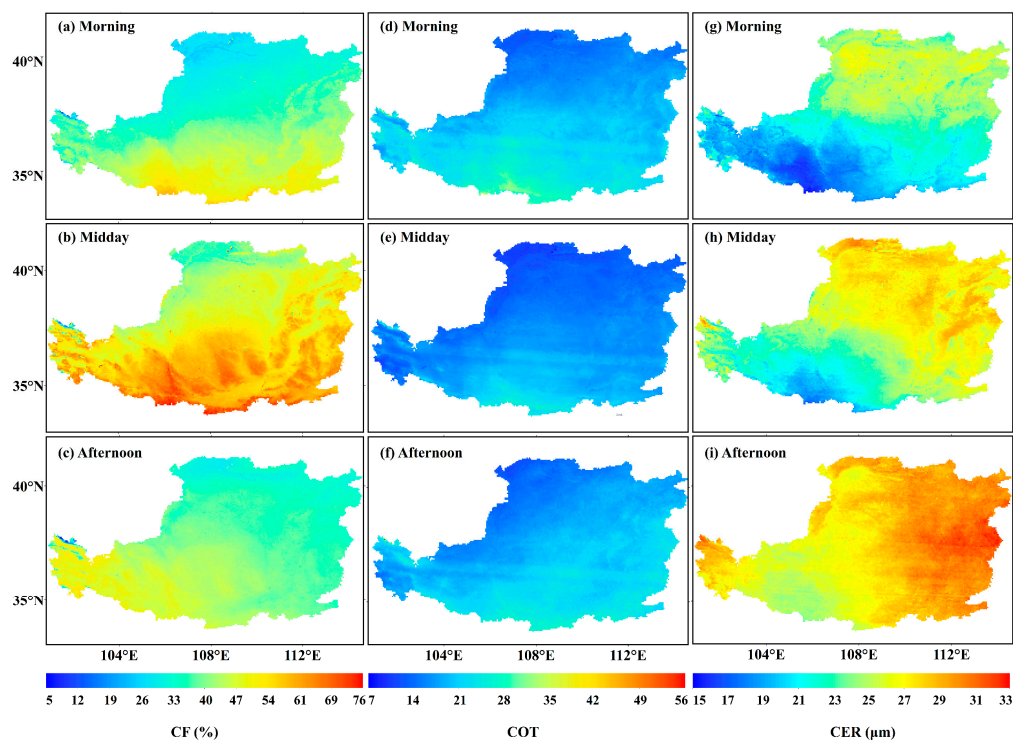


Figure 4. Spatial distribution of diurnal variations in CF, COT and CER in the Loess Plateau. (a–c) CF. (d–f) COT. (g–i) CER.

Overall, both in terms of spatial and temporal variation, CF, COT and CER exhibited significant differences. The spatial distributions of CF, COT and CER generally presented clear north–south contrast patterns. High values of CF and COT were observed in the southern Loess Plateau, where low values of CER were observed. The CF value in summer was much higher than that in other seasons, and the difference in the CF between the

north and the south part of Loess Plateau was small in summer. Meanwhile, the highest COT value was observed in autumn, and the highest COT values mainly appeared in the southern Loess Plateau. In spring and winter, the CER values were higher than those in other seasons, and the areas with the highest CER values were mainly in the northern Loess Plateau. Regarding the diurnal variation in cloud properties, the CF values were low in the morning and afternoon and high at midday. The COT values were high in the morning and afternoon and low at noon. In contrast, the CER values showed an increasing trend from 7:00 BJT to 17:00 BJT and reached a maximum at 17:00 BJT. Moreover, the intra-day time variation was consistent with the intra-day spatial variation.

4. Discussion

Based on the spatial distribution of cloud properties, the CF and COT values showed clear patterns, being high in the south and low in the north of the Loess Plateau. The formation and development of clouds is closely related to the water vapor status and stability of the environmental atmosphere [37]. After the implementation of projects returning farmland to forests and grasslands in the Loess Plateau, the vegetation coverage significantly improved in most areas, but vegetation coverage still shows a pattern of being high over the southeastern Loess Plateau and relatively low over the northwestern Loess Plateau [28,38]. Although atmospheric circulation mainly influences the atmospheric water vapor over a region, Zhang et al. [39] pointed out that the increase in vegetation contributed 37.40% of the increase in precipitation over the Loess Plateau, compared with external atmospheric circulation changes, which contributed about 62.60%. General atmospheric circulation patterns and environmental conditions both influence cloud formation and precipitation. Vegetation influences cloud formation by influencing the temperature, soil moisture and evapotranspiration, which ultimately influence the amount of water vapor delivered to the atmosphere [40–42]. Therefore, to explore the potential surface water and heat condition factors for the cloud distribution pattern over the Loess Plateau, we calculated the annual and seasonal mean total column water vapor (TCWV) and its related parameters of temperature (TMP), normalized difference vegetation index (NDVI) and potential evapotranspiration (PET); these are shown in Figure 5. By comparing the annual and seasonal spatial distribution of CF with the NDVI and total column water vapor, we found that they showed similar patterns, especially in summer (Figure 5h,r). The annual average potential evapotranspiration also increased from northwest to southeast (Figure 5k), presenting the same pattern as CF distribution. Moreover, the temperature of the Loess Plateau was also high in the south and low in the north (Figure 5a), which relates to evapotranspiration and soil moisture, which influence the water vapor content in the atmosphere.

To further quantify the relationship between surface water and heat conditions and cloud frequency, we used Geodetector, which provides reasonable and explainable results to understand the spatial patterns of variables, as shown in Figure 6a. We quantified the contribution of the total column water vapor, NDVI, temperature and potential evapotranspiration on CF at the annual scale. The factor detection results show that the total column water vapor (with a q-statistic of 0.44) and the NDVI (with a q-statistic of 0.38) are the most powerful factors in the explanation of CF. However, interaction detection showed that interactions of temperature and potential evapotranspiration with the total column water vapor had a larger impact on cloud frequency, with q-statistics of 0.65 and 0.74, respectively. The statistical results from Geodetector show that the dominant factors in cloud distribution are total column water vapor and NDVI. However, interactions between temperature and potential evapotranspiration, and total column water vapor both have significant influences on cloud distribution. Overall, all surface water and heat indicators showed similar spatial patterns to cloud frequency, and the statistical results also enhanced the relationship between these variables and cloud frequency. Therefore, we can conclude that surface water and heat conditions influence the cloud patterns over the Loess Plateau to some extent.

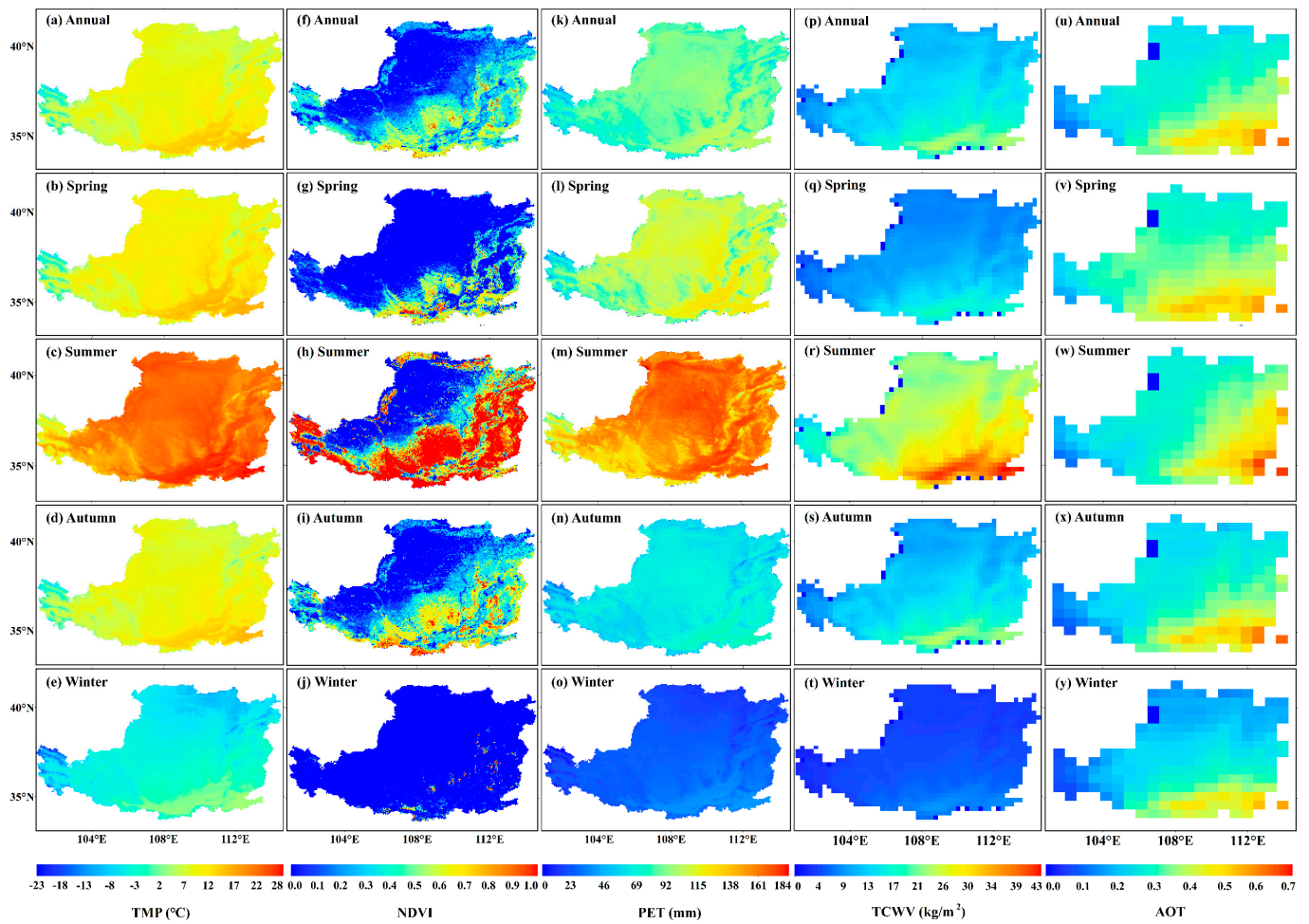


Figure 5. Spatial distribution of annual and seasonal variations in average temperature (TMP), NDVI, potential evapotranspiration (PET), total column water vapor (TCWV) and aerosol optical thickness (AOT) in the Loess Plateau. (a–e) Annual and seasonal mean of TMP. (f–j) Annual and seasonal mean of NDVI. (k–o) Annual and seasonal mean of PET. (p–t) Annual and seasonal mean of TCWV. (u–y) Annual and seasonal mean of AOT.

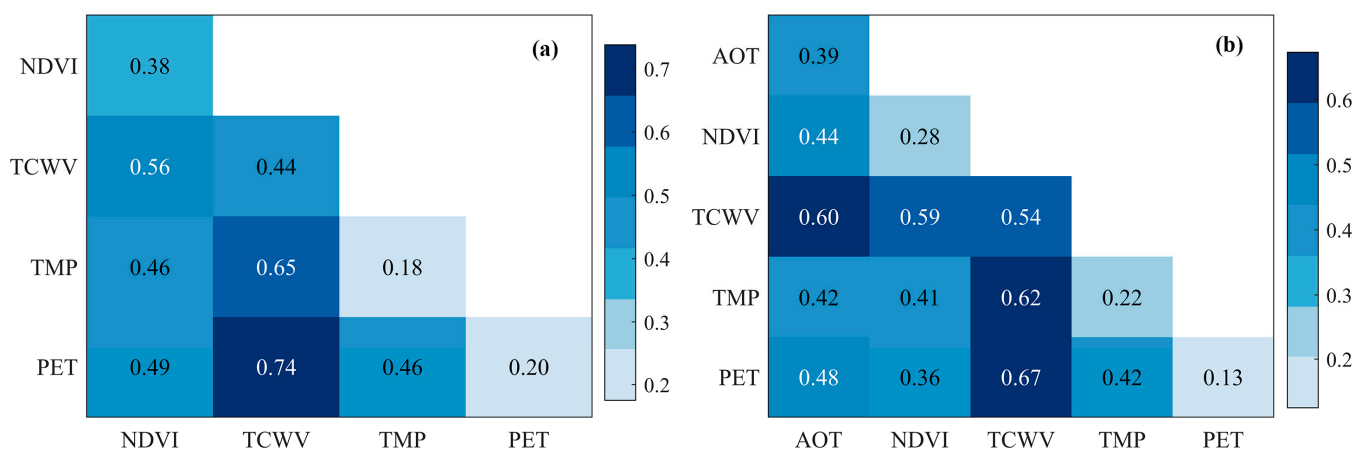


Figure 6. Interaction detection of influence factors based on Geodetector for CF (a) and COT (b).

We also selected two typical regions over the Loess Plateau in which the NDVI and total column water vapor over areas were different to explore the relationship between

surface conditions and cloud frequency. The locations of the two regions, A and B, are shown in Figure 1. Region A is in the northern Loess Plateau and is a desert area with low vegetation cover, and region B is located in the southern Loess Plateau, where the NDVI and total column water vapor values are relatively high. Based on Figure 5a,f,k, region A had a lower temperature, NDVI and potential evapotranspiration than region B. Theoretically, the CF value in region B, where the total column water vapor was relatively high, was significantly higher than that in region A. The comparison of CF in Figure 7a indicates the same results: the CF value in region B is much higher than that in region A. Comparing diurnal variation in CF in different seasons (Figure 7b), it can be concluded that the CF value was higher in summer than in autumn in region A; however, it was different in region B, where the CF value was very similar in summer and autumn. We calculated the total column water vapor in summer and autumn; the values were 21.93 kg/m² and 9.90 kg/m² in region A and 32.58 kg/m² and 19.33 kg/m² in region B. The discrepancy rate of total column water vapor in summer and autumn was higher in region A than in region B, and total column water vapor values for region B were high in summer and autumn. Although the water vapor in region A was relatively low in summer, the soil in region A was loose and porous, and the permeability was low, which means that water evaporated easily [43,44]. In addition, the temperature (Figure 5c) and rainfall reached the maximum values in summer, and the rising temperature increased the amount of water vapor in the atmosphere, leading to cloud formation, which contributed to the high CF value in summer [45,46].

In addition, the CF value in the whole Loess Plateau was also high in the summer. Based on Figure 5q–t, the total column water vapor values for the four seasons in the whole Loess Plateau were 5.91 kg/m², 15.35 kg/m², 7.71 kg/m² and 2.48 kg/m², respectively, which indicated that the water vapor in summer was much larger than that in other seasons, creating good conditions for the formation of clouds. Regarding the diurnal variation in clouds, the CF value was greater at midday than in the morning and afternoon. This may have been related to the rapidly rising temperature at midday; a rising temperature leads to warm air rising, expanding and cooling. Finally, it will cool off to create condensation, at which point water vapor turns into clouds.

The analysis in Section 3 indicates that the COT value was higher in the southern Loess Plateau. COT is closely related to water vapor content, temperature and aerosol optical thickness [47]. Gao [48] found that with an increase in aerosol optical thickness (AOT), the COT value showed an increasing trend in the Loess Plateau. Aerosols contribute to higher cloud droplet number concentration, leading to higher COT values [49]. We calculated the seasonal and annual mean values of the aerosol optical thickness (Figure 5u–y). Based on Figure 5u, the aerosol optical thickness was high in the southern Loess Plateau. We also can see from Figure 5p that the southern part of the Loess Plateau had a high total column water vapor value. As such, the high total column water vapor and aerosol optical thickness values may have been the reason for the high COT value in the southern Loess Plateau. We also used Geodetector to quantify the influence of total column water vapor, aerosol optical thickness, NDVI, temperature and potential evapotranspiration and the interaction between these variables on COT (Figure 6b). The results show that the q-statistics were 0.54 and 0.39 for total column water vapor and aerosol optical thickness, respectively. In addition, interaction detection showed that the interactions between potential evapotranspiration and total column water vapor (with a q-statistic of 0.67), temperature and total column water vapor (with a q-statistic of 0.62) and total column water vapor and aerosol optical thickness (with a q-statistic of 0.60) showed larger q-statistics than one variable. The statistical results also indicate that the total column water vapor and aerosol optical thickness are the main factors affecting COT, and the interaction between total column water vapor and other factors will also have a great influence on the COT. In addition, we also found that the diurnal variation was characterized by greater COT values in the morning and afternoon. One reason for this may have been the lower temperatures in the morning and the strong

radiation cooling in the afternoon which promote the condensation of water vapor to form clouds when the water vapor in the air exceeds the saturation state [50–53].

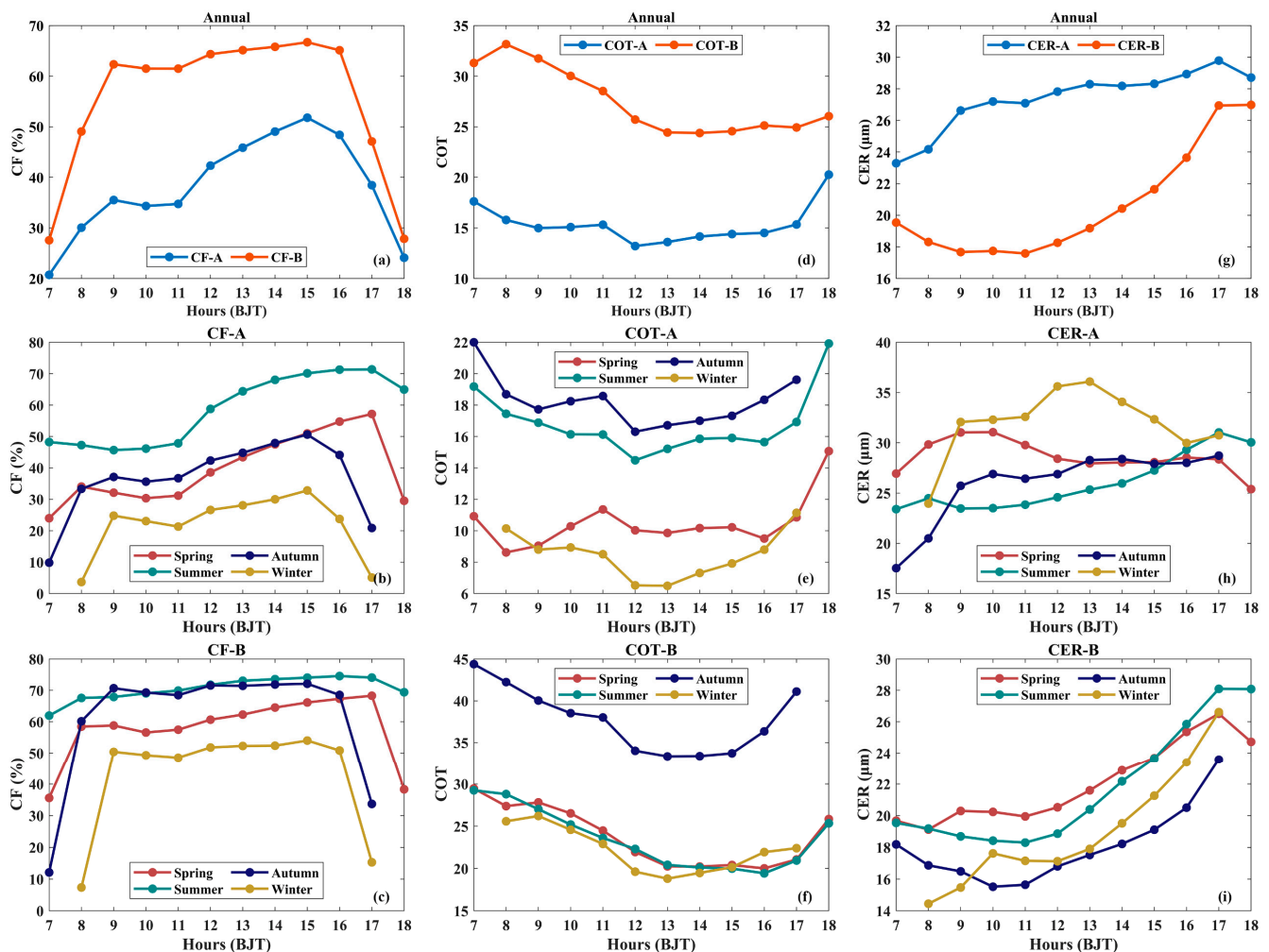


Figure 7. The diurnal variations in CF, COT, and CER in the Loess Plateau in the two subregions. (a–c) Annual and seasonal mean of CF in regions A and B. (d–f) Annual and seasonal mean of COT in regions A and B. (g–i) Annual and seasonal mean of CER in regions A and B.

The pattern of CER contrasted with that of CF and COT. The CER values were larger in the northern Loess Plateau and relatively small in the southern Loess Plateau (Figure 2k). The CER was mainly influenced by aerosols, water vapor and thermal stability [54]. From Figure 5p,a, we can find that the total column water vapor and temperature are relatively small in the northern Loess Plateau. Based on Figure 7g, the CER value in region A was greater than in region B in the daytime. Region A is a desert area, and the total column water vapor, as well as the temperature, was relatively low. High values of CER in region A were mainly observed in spring and winter (Figure 7h). We also calculated ice cloud and water cloud frequency over the Loess Plateau based on CloudSat data in 2015 (see Figure 8). From Figure 8, there was a higher frequency of ice clouds over the northern Loess Plateau than over the southern area. Ice clouds also occurred more often in spring and winter, especially in the northern part of the Loess Plateau. This could have been associated with the colder temperature (Figure 5b,e) in spring and winter and the higher nucleation rate [55,56]. In addition, more dust and pollutants produced by human activities are present in the air in spring and winter because of sandstorms in spring and the use of heating in winter. They combine with water vapor and form large and dense cloud particles more easily. Over region B, in contrast, the CER values were larger in spring and summer (Figure 7i), which

was more likely related to the sufficient water vapor and high aerosol optical thickness in spring and summer in region B [56]. However, Zhao et al. [57], Qiu et al. [58] and Jung et al. [59] found that CER is closely associated with the aerosol type, aerosol amount, cloud type, and water vapor, and their relationship is complicated. For example, aerosols as cloud condensation nuclei affect the CER value [49]. Moreover, the influence of aerosols on CER is also related to the environment [60]. Gao [48] found that the water cloud effective radius increased with increasing aerosol optical thickness, while the ice cloud effective radius was negatively correlated with aerosol optical thickness in the Loess Plateau. Under different cloud water content levels, CER showed different relationships with aerosol optical thickness [61]. Thus, the relationship between these influence factors and CER needs to be investigated further. Therefore, this analysis provides limited insight into the influence of different parameters on cloud parameters; it cannot be used to demonstrate a strong causal relationship between them.

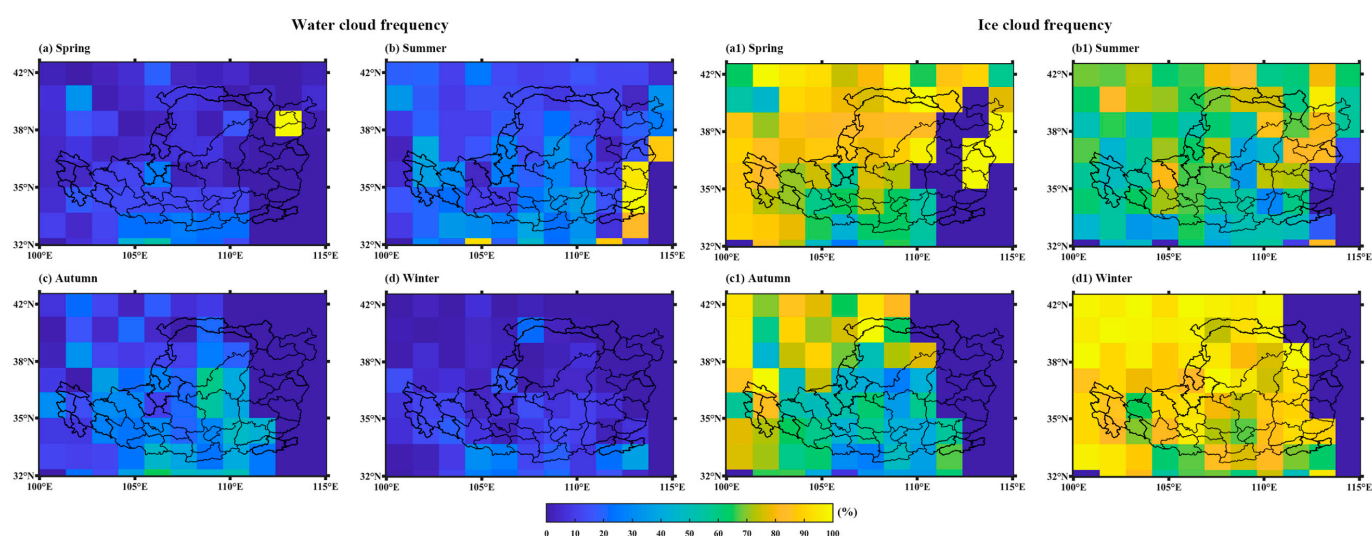


Figure 8. Spatial distribution of cloud phase frequencies over the Loess Plateau. (a–d) Spatial distribution of water cloud frequency in four seasons. (a1–d1) Spatial distribution of ice cloud frequency in four seasons.

5. Conclusions

Clouds play a vital role in the climate system, water cycle and surface solar radiation simulation and prediction, especially in arid and semi-arid regions, where clouds are potentially sustainable water resources. The macro- and micro-physical properties of clouds have regional characteristics that influence the local radiation budget, climate and meteorology. This paper analyzed the temporal and spatial characteristics in cloud frequency (CF), cloud optical thickness (COT) and cloud effective radius (CER) in the Loess Plateau based on H-8 satellite cloud products from July 2015 to February 2022.

On both the annual and seasonal scales, all three parameters showed clear north–south discrepancies in space. The spatial distribution of CF had distinct features, with higher values in the southern Loess Plateau and lower values in the northern Loess Plateau. However, the spatial differences between the four seasons were obvious. The CF values were highest in summer and lowest in winter. The COT values showed similar patterns with CF: high values were observed in the southern Loess Plateau, and low values were observed in the northern Loess Plateau. Higher COT values were observed in autumn, and lower COT values were observed in winter. In addition, the spatial distribution of CER showed the opposite pattern to CF and COT. The CER in the northern and southern parts of the Loess Plateau reached the maximum and minimum annual average values, respectively. The largest CER value was observed in winter. In terms of the diurnal variations, the CF value was low in the morning and afternoon and high at noon, and the CF value was the

highest at around 15:00 BJT. However, the diurnal variation in COT showed the opposite pattern to CF, being high in the morning and afternoon and lower at midday. The CER values increased between 7:00 BJT and 17:00 BJT. The maximum value of CER appeared at 17:00 BJT.

The potential reasons for the regional cloud characteristics over the Loess Plateau were also explored further. By comparing CF values with the normalized difference vegetation index, total column water vapor, potential evapotranspiration and temperature over the Loess Plateau, we found that CF showed a similar spatial distribution to these variables, and all of them had high values in the southern part of the Loess Plateau. Based on the results of factor detection and interactive detection modules from Geodetector, we also found that the total column water vapor, normalized difference vegetation index, temperature and potential evapotranspiration have great explanatory power for CF. Therefore, large CF values in the southern Loess Plateau are related to surface water and heat conditions. The higher COT value in the southern Loess Plateau was consistent with the sufficient water vapor and high aerosol optical thickness in this area. However, the large value of the CER in the northern part of the Loess Plateau and in spring and winter may have been associated with the higher nucleation rate caused by colder temperatures. Water vapor and aerosols also influence the CER, but they have complex relationships with it. In terms of diurnal variations, the low CF values in the morning and high values at noon could be explained by the fact that the temperature rapidly rose, and the water vapor values were sufficient at midday. However, the diurnal variation in COT showed the opposite pattern to that of CF. The high COT values in the morning and afternoon might have been affected by the low temperature in the morning and the intense radiation cooling in the afternoon.

This paper studied the temporal and spatial variation characteristics of cloud properties over the Loess Plateau. The potential reasons for the regional cloud characteristics over the Loess Plateau were also analyzed, but the explanation for the temporal and spatial characteristics in cloud properties was not comprehensive enough, and future research needs to be carried out so that we can better understand the physical and dynamic reasons behind these temporal and spatial features in cloud properties.

Author Contributions: Conceptualization, S.Z. and C.J.; methodology, S.Z., C.J., Q.T., X.D. and G.M.; data processing, C.J., Q.T. and X.D.; writing—original draft preparation, S.Z., C.J., Q.T. and G.M.; writing—review and editing, S.Z., C.J., Q.T., X.D. and G.M.; supervision, S.Z. All authors have read and agreed to the published version of the manuscript.

Funding: This work was supported by the Scientific Research Project of Shaanxi Provincial Education Department (Grant No. 21JK0770), National Natural Science Foundation of China (Grant Nos. 41701442, 41977059 and 52109031).

Data Availability Statement: The cloud optical thickness and cloud effective radius data are from the Japan Aerospace Exploration Agency (JAXA). They are available at <https://www.eorc.jaxa.jp/ptree/>, accessed on 19 June 2022, while the cloud phase data is available at <http://www.cloudsat.cira.colostate.edu/>, accessed on 16 November 2022. The total column water vapor data can be obtained from <https://cds.climate.copernicus.eu/>, accessed on 9 January 2023. The aerosol optical thickness data is available at <https://disc.gsfc.nasa.gov/>, accessed on 6 January 2023. The NDVI data is available at <https://ladsweb.modaps.eosdis.nasa.gov/>, accessed on 27 November 2022. The temperature and potential evapotranspiration data are from National Tibetan Plateau Data Center. They are available at <http://data.tpdc.ac.cn/>, accessed on 26 November 2022.

Acknowledgments: The authors would like to acknowledge the Japan Aerospace Exploration Agency (JAXA) for providing Himawari-8 satellite products, the National Tibetan Plateau Data Center for providing China's monthly average temperature and potential evapotranspiration data, the European Center for Mesoscale Weather Forecasting (ECMWF) and National Aeronautics and Space Administration (NASA) for providing atmospheric reanalysis data and NASA's MODIS satellite for providing the NDVI product.

Conflicts of Interest: The authors declare no conflict of interest.

References

1. Stubenrauch, C.J.; Cros, S.; Guignard, A.; Lamquin, N. A 6-year global cloud climatology from the Atmospheric InfraRed Sounder AIRS and a statistical analysis in synergy with CALIPSO and CloudSat. *Atmos. Chem. Phys.* **2010**, *10*, 7197–7214. [[CrossRef](#)]
2. Ramanathan, V.; Cess, R.D.; Harrison, E.F.; Minnis, P.; Barkstrom, B.R.; Ahmad, E.; Hartmann, D. Cloud-radiative forcing and climate: Results from the earth radiation budget experiment. *Science* **1989**, *243*, 57–63. [[CrossRef](#)]
3. Abbood, Z.M.; Al-Taai, O.T. Calculation of absorption and emission of thermal radiation by clouds cover. *ARPN J. Eng. Appl. Sci.* **2018**, *13*, 9446–9456.
4. Gettelman, A.; Sherwood, S.C. Processes responsible for cloud feedback. *Curr. Clim. Change Rep.* **2016**, *2*, 179–189. [[CrossRef](#)]
5. Wang, M.; Su, J.; Xu, Y.; Han, X.; Peng, N.; Ge, J. Radiative contributions of different cloud types to regional energy budget over the SACOL site. *Clim. Dyn.* **2023**, *60*, 1–19. [[CrossRef](#)]
6. Li, Y.; Yu, R.; Xu, Y.; Zhang, X. Spatial distribution and seasonal variation of cloud over China based on ISCCP data and surface observations. *J. Meteorol. Ser. II* **2004**, *82*, 761–773. [[CrossRef](#)]
7. Yang, Y.; Zhao, C.; Fan, H. Spatiotemporal distributions of cloud properties over China based on Himawari-8 advanced Himawari imager data. *Atmos. Res.* **2020**, *240*, 104927. [[CrossRef](#)]
8. Shields, J.E.; Karr, M.E.; Johnson, R.W.; Burden, A.R. Day/night whole sky imagers for 24-h cloud and sky assessment: History and overview. *Appl. Opt.* **2013**, *52*, 1605–1616. [[CrossRef](#)]
9. Rossow, W.B. *History of the International Satellite Cloud Climatology Project*; World Climate Research Programme (WCRP): Geneva, Switzerland, 2022. [[CrossRef](#)]
10. Wielicki, B.A.; Barkstrom, B.R.; Harrison, E.F.; Lee, R.B.; Louis Smith, G.L.; Cooper, J.E. Clouds and the Earth's Radiant Energy System (CERES): An earth observing system experiment. *Bull. Am. Meteor. Soc.* **1996**, *77*, 853–868. [[CrossRef](#)]
11. Sun, M.; Doelling, D.R.; Loeb, N.G.; Scott, R.C.; Wilkins, J.; Nguyen, L.T.; Mlynarczyk, P. Clouds and the Earth's radiant energy system (CERES) FluxByCldTyp edition 4 data product. *J. Atmos. Oceanic Technol.* **2022**, *39*, 303–318. [[CrossRef](#)]
12. Kondragunta, C.R.; Gruber, A. Seasonal and annual variability of the diurnal cycle of clouds. *J. Geophys. Res-Atmos.* **1996**, *101*, 21377–21390. [[CrossRef](#)]
13. Cintineo, J.L.; Pavlonis, M.J.; Sieglaff, J.M.; Heidinger, A.K. Evolution of severe and nonsevere convection inferred from GOES-derived cloud properties. *J. Appl. Meteor. Climatol.* **2013**, *52*, 2009–2023. [[CrossRef](#)]
14. Senf, F.; Dietzsch, F.; Hünerbein, A.; Deneke, H. Characterization of initiation and growth of selected severe convective storms over central Europe with MSG-SEVIRI. *J. Appl. Meteor. Climatol.* **2015**, *54*, 207–224. [[CrossRef](#)]
15. Shang, H.; Letu, H.; Nakajima, T.Y.; Wang, Z.; Ma, R.; Wang, T.; Lei, Y.; Ji, D.; Li, S.; Shi, J. Diurnal cycle and seasonal variation of cloud cover over the Tibetan Plateau as determined from Himawari-8 new-generation geostationary satellite data. *Sci. Rep.* **2018**, *8*, 1105. [[CrossRef](#)]
16. Winker, D.M.; Hunt, W.H.; McGill, M.J. Initial performance assessment of CALIOP. *Geophys. Res. Lett.* **2007**, *34*, L19803. [[CrossRef](#)]
17. Mace, G.G.; Zhang, Q.; Vaughan, M.; Marchand, R.; Stephens, G.; Trepte, C.; Winker, D. A description of hydrometeor layer occurrence statistics derived from the first year of merged Cloudsat and CALIPSO data. *J. Geophys.* **2009**, *114*, D00A26. [[CrossRef](#)]
18. Wang, J.; Jian, B.; Wang, G.; Zhao, Y.; Li, Y.; Letu, H.; Zhang, M.; Li, J. Climatology of cloud phase, cloud radiative effects and precipitation properties over the Tibetan Plateau. *Remote Sens.* **2021**, *13*, 363. [[CrossRef](#)]
19. Chen, J.; Wu, X.; Yin, Y.; Huang, Q.; Xiao, H. Characteristics of cloud systems over the Tibetan Plateau and East China during boreal summer. *J. Climate* **2017**, *30*, 3117–3137. [[CrossRef](#)]
20. Li, L.; Sun, M.; Mei, J. Variation and influencing factors of cloud characteristics over Qinghai lake from 2006 to 2019. *Sustainability* **2022**, *14*, 11935. [[CrossRef](#)]
21. Liu, J. Analysis on cloud microphysical property over Qinghai-Xizang Plateau using satellite data. *Plateau Meteor.* **2013**, *32*, 38–45. (In Chinese)
22. Zhou, R.; Wang, G.; Zhaxi, S. Cloud vertical structure measurements from a ground-based cloud radar over the southeastern Tibetan Plateau. *Atmos. Res.* **2021**, *258*, 105629. [[CrossRef](#)]
23. Liu, W.; Sang, T. Potential productivity of the Miscanthus energy crop in the Loess Plateau of China under climate change. *Environ. Res. Lett.* **2013**, *8*, 044003. [[CrossRef](#)]
24. He, P.; Ma, J.; Han, Z.; Shi, M.; Xu, D.; Sun, Z. Relationship between multi-scale climate factors and performance of ecological engineering on the Loess Plateau, China. *J. For. Res.* **2021**, *33*, 789–800. [[CrossRef](#)]
25. Li, S.; Liang, W.; Fu, B.; Lu, Y.; Fu, S.; Wang, S.; Su, H. Vegetation changes in recent large-scale ecological restoration projects and subsequent impact on water resources in China's Loess Plateau. *Sci. Total. Environ.* **2016**, *569–570*, 1032–1039. [[CrossRef](#)] [[PubMed](#)]
26. Sun, W.; Song, X.; Mu, X.; Gao, P.; Wang, F.; Zhao, G. Spatiotemporal vegetation cover variations associated with climate change and ecological restoration in the Loess Plateau. *Agric. Forest Meteorol.* **2015**, *209–210*, 87–99. [[CrossRef](#)]
27. An, S.; Cheng, M.; Xue, Z.; Ma, R. Current State of Multifunctional Use of Grasslands. In *Multifunctional Land-Use Systems for Managing the Nexus of Environmental Resources*; Zhang, L., Schwärzel, K., Eds.; Springer: Cham, Switzerland, 2017; pp. 69–77. [[CrossRef](#)]
28. Yan, M.J.; He, Q.Y.; Yamanaka, N.; Du, S. Location, Geology and Landforms of the Loess Plateau. In *Restoration and Development of the Degraded Loess Plateau, China*; Tsunekawa, A., Liu, G., Yamanaka, N., Du, S., Eds.; Springer: Tokyo, Japan, 2014; pp. 3–21. [[CrossRef](#)]

29. Li, Z.; Zheng, F.; Liu, W.; Flanagan, D.C. Spatial distribution and temporal trends of extreme temperature and precipitation events on the Loess Plateau of China during 1961–2007. *Quat. Int.* **2010**, *226*, 92–100. [[CrossRef](#)]
30. Bi, J.; Huang, J.; Fu, Q.; Wang, X.; Shi, J.; Zhang, W.; Huang, Z.; Zhang, B. Toward characterization of the aerosol optical properties over Loess Plateau of northwestern China. *J. Quant. Spectrosc. Ra.* **2011**, *112*, 346–360. [[CrossRef](#)]
31. Fang, W.; Huang, S.; Huang, Q.; Huang, G.; Wang, H.; Leng, G.; Wang, L.; Guo, Y. Probabilistic assessment of remote sensing-based terrestrial vegetation vulnerability to drought stress of the Loess Plateau in China. *Remote Sens. Environ.* **2019**, *232*, 111290. [[CrossRef](#)]
32. Letu, H.; Nakajima, T.Y.; Wang, T.; Shang, H.; Ma, R.; Yang, K.; Baran, A.J.; Riedi, J.; Ishimoto, H.; Yoshida, M.; et al. A new benchmark for surface radiation products over the East Asia–Pacific region retrieved from the Himawari-8/AHI next-generation geostationary satellite. *Bull. Amer. Meteor. Soc.* **2022**, *103*, E873–E888. [[CrossRef](#)]
33. Bessho, K.; Date, K.; Hayashi, M.; Ikeda, A.; Imai, T.; Inoue, H.; Kumagai, Y.; Miyakawa, T.; Murata, H.; Ohno, T.; et al. An introduction to Himawari-8/9—Japan’s new-generation geostationary meteorological satellites. *J. Meteorol. Ser. II* **2016**, *94*, 151–183. [[CrossRef](#)]
34. Yamamoto, Y.; Ichii, K.; Higuchi, A.; Takenaka, H. Geolocation accuracy assessment of Himawari-8/AHI imagery for application to terrestrial monitoring. *Remote Sens.* **2020**, *12*, 1372. [[CrossRef](#)]
35. Wang, J.F.; Xu, C.D. Geodetector: Principles and prospects. *Acta Geol. Sin.* **2017**, *72*, 116–134. (In Chinese)
36. Wang, H.; Qin, F.; Xu, C.; Li, B.; Guo, L.; Wang, Z. Evaluating the suitability of urban development land with a Geodetector. *Ecol. Indic.* **2021**, *123*, 107339. [[CrossRef](#)]
37. Liu, J.J.; Chen, B.D. Cloud occurrence frequency and structure over the Qinghai-Tibetan Plateau from CloudSat observation. *Plateau Meteor.* **2017**, *36*, 632–642. (In Chinese)
38. Zhao, H.; He, H.; Wang, J.; Bai, C.; Zhang, C. Vegetation restoration and its environmental effects on the loess plateau. *Sustainability* **2018**, *10*, 4676. [[CrossRef](#)]
39. Zhang, B.; Tian, L.; Zhao, X.; Wu, P. Feedbacks between vegetation restoration and local precipitation over the loess plateau in China. *Sci. China Earth Sci.* **2021**, *64*, 920–931. (In Chinese) [[CrossRef](#)]
40. Zhao, Q.; Ma, X.; Liang, L.; Yao, W. Spatial-temporal variation characteristics of multiple meteorological variables and vegetation over the Loess Plateau region. *Appl. Sci.* **2020**, *10*, 1000. [[CrossRef](#)]
41. Yang, Z.; Zhang, Q.; Hao, X. Evapotranspiration trend and its relationship with precipitation over the Loess Plateau during the last three decades. *Adv. Meteorol.* **2016**, *2016*, 6809749. [[CrossRef](#)]
42. Zhao, W.; Fang, X.; Daryanto, S.; Zhang, X.; Wang, Y. Factors influencing soil moisture in the Loess Plateau, China: A review. *Earth Environ. Sci. Trans. R. Soc. Edinb.* **2018**, *109*, 501–509. [[CrossRef](#)]
43. Zhuang, J.; Peng, J.; Wang, G.; Javed, I.; Wang, Y.; Li, W. Distribution and characteristics of landslide in Loess Plateau: A case study in Shaanxi province. *Eng. Geol.* **2018**, *236*, 89–96. [[CrossRef](#)]
44. Liu, J.; Li, X.; Xue, Q.; Guo, Z. Experimental study on air permeability and microscopic mechanism of intact and remolded Malan loess, Loess Plateau, China. *Bull. Eng. Geol. Environ.* **2020**, *79*, 3909–3919. [[CrossRef](#)]
45. Qin, J.; Duan, W.; Chen, Y.; Dukhovny, V.A.; Sorokin, D.; Li, Y.; Wang, X. Comprehensive evaluation and sustainable development of water–energy–food–ecology systems in Central Asia. *Renew. Sust. Energ. Rev.* **2022**, *157*, 112061. [[CrossRef](#)]
46. Duan, W.; Maskey, S.; Chaffe, P.L.B.; Luo, P.; He, B.; Wu, Y.; Hou, J. Recent advancement in remote sensing technology for hydrology analysis and water resources management. *Remote Sens.* **2021**, *13*, 1097. [[CrossRef](#)]
47. Zhou, X.X.; Zhang, H.; Jing, X.W. Distribution and variation trends of cloud amount and optical thickness over China. *J. Atmos. Environ. Opt.* **2016**, *11*, 1–13. (In Chinese)
48. Gao, X.X. Optical properties and climatic effects of aerosols in representative regions over China. Ph.D. Thesis, Lanzhou University, Lanzhou, China, 2018. (In Chinese)
49. Albrecht, B.A. Aerosols, cloud microphysics, and fractional cloudiness. *Science* **1989**, *245*, 1227–1230. [[CrossRef](#)] [[PubMed](#)]
50. Li, Y.; Yi, B.; Min, M. Diurnal variations of cloud optical properties during day-time over China based on Himawari-8 satellite retrievals. *Atmos. Environ.* **2022**, *277*, 1352–2310. [[CrossRef](#)]
51. Roeckner, E.; Schlese, U.; Biercamp, J.; Loewe, P. Cloud optical depth feedbacks and climate modelling. *Nature* **1987**, *329*, 138–140. [[CrossRef](#)]
52. Li, X.; Che, H.; Wang, H.; Xia, X.; Chen, Q.; Gui, K.; Zhao, H.; An, L.; Zheng, Y.; Sun, T.; et al. Spatial and temporal distribution of the cloud optical depth over China based on MODIS satellite data during 2003–2016. *J. Environ. Sci.* **2019**, *80*, 66–81. [[CrossRef](#)]
53. Harrison, R.G. Cloud formation and the possible significance of charge for atmospheric condensation and ice nuclei. *Space Sci. Rev.* **2000**, *94*, 381–396. [[CrossRef](#)]
54. Yang, D.S.; Wang, P.C. Tempo-spatial distribution characteristics of cloud particle size over china during summer. *Clim. Environ. Res.* **2012**, *17*, 433–443. (In Chinese)
55. Coopman, Q.; Riedi, J.; Finch, D.P.; Garrett, T.J. Evidence for changes in arctic cloud phase due to long-range pollution transport. *Geophys. Res. Lett.* **2018**, *45*, 10–709. [[CrossRef](#)]
56. Zhao, C.; Chen, Y.; Li, J.; Letu, H.; Su, Y.; Chen, T.; Wu, X. Fifteen-year statistical analysis of cloud characteristics over China using Terra and Aqua Moderate Resolution Imaging Spectroradiometer observations. *Int. J. Climatol.* **2019**, *39*, 2612–2629. [[CrossRef](#)]
57. Zhao, C.F.; Klein, S.A.; Xie, S.; Liu, X.; Boyle, J.S.; Zhang, Y. Aerosol first indirect effects on non-nrcinitatine low-level lioud cloud nronerties as simulated by CAMs at ARM sites. *Geophys. Res. Lett.* **2012**, *39*, L08806. [[CrossRef](#)]

58. Qiu, Y.M.; Zhao, C.F.; Guo, J.P.; Li, J.M. 8-year ground-based observational analysis about the seasonal variation of the aerosol-cloud droplet effective radius relationship at SGP site. *Atmos. Environ.* **2017**, *164*, 139–146. [[CrossRef](#)]
59. Jung, W.S.; Panicker, A.; Lee, D.I.; Park, S.H. Estimates of aerosol indirect effect from terra MODIS over Republic of Korea. *Adv. Meteorol.* **2013**, *2013*, 976813. [[CrossRef](#)]
60. Douglas, A.R. The Effects of Aerosol-Cloud Interactions on Warm Cloud Properties. Ph.D. Thesis, The University of Wisconsin, Madison, WI, USA, 2020.
61. Li, Z.; Wang, Y.; Guo, J.; Zhao, C.; Cribb, M.C.; Dong, X.; Fan, J.; Gong, D.; Huang, J.; Jiang, M.; et al. East Asian study of tropospheric aerosols and their impact on regional clouds, precipitation, and climate (EAST-AIRCPC). *J. Geophys. Res. Atmos.* **2019**, *124*, 13026–13054. [[CrossRef](#)]

Disclaimer/Publisher’s Note: The statements, opinions and data contained in all publications are solely those of the individual author(s) and contributor(s) and not of MDPI and/or the editor(s). MDPI and/or the editor(s) disclaim responsibility for any injury to people or property resulting from any ideas, methods, instructions or products referred to in the content.